Geochimica et Cosmochimica Acta 365 (2024) 101–113

Contents lists available at ScienceDirect

Geochimica et Cosmochimica Acta

journal homepage: www.elsevier.com/locate/gca

The effect of water on alkali trace element diffusion (Li, Rb, Cs) in silicic melts

Juliana Troch [a,b,*], Christian Huber [c], Nico Kueter [d,e], Marcel Guillong [e], Mike Ackerson [b], Peter Ulmer [e], Olivier Bachmann [e]

[a] Faculty of Georesources and Material Sciences, RWTH Aachen University, 57072 Aachen, Germany
[b] Department of Mineral Sciences, Smithsonian National Museum of Natural History, Washington DC 20560, USA
[c] Department of Earth, Environmental and Planetary Sciences, Brown University, Providence RI 02912, USA
[d] Earth and Planets Laboratory, Carnegie Institution of Science, Washington DC 20008, USA
[e] Department of Earth Sciences, ETH Zurich, 8092 Zurich, Switzerland

ARTICLE INFO

Associate editor: James Van Orman

Keywords:
Diffusion
Water
Melt
Trace elements

ABSTRACT

Trace element diffusion is a powerful tracer of kinetic magmatic processes such as recharge and fluid exsolution. However, the dependence of diffusivities (D) on melt water contents is poorly quantified, and most trace element diffusivities were determined in water-free melts unrealistic for most natural magmatic systems. Here, we investigate the diffusion of the alkali trace elements Li, Rb, and Cs as a function of water content in rhyodacite, high-silica rhyolite, and peralkaline rhyolite. For the diffusion experiments, homogenous hydrous glass cylinders were produced from trace element-doped and undoped powdered glass with 1–8 wt% H_2O. Glass cylinders with the same water content but different trace element concentrations were paired along polished contact surfaces. Diffusion experiments were conducted between 720 and 1100 °C at 100–700 MPa for 5–25 min using gas pressure vessels or a piston cylinder apparatus. Resulting diffusion profiles were analyzed by LA-ICPMS and evaluated by a Monte Carlo iterative fitting procedure for full error propagation. At a given experimental temperature, measured $log_{10}D$ values increase linearly with melt water content, with one order of magnitude increase for Li, two orders for Rb, and three orders for Cs from least hydrous (1 wt%) to wettest (8 wt%) experiment, due to a linear decrease in activation energies. Variations in major element composition only have a minor effect. We illustrate the impact of differential diffusion in hydrous silicic magmas on their trace element budget by coupling our data to a two-phase mechanical model of channelized fluid transport in magmatic systems. Quantifying water-dependent diffusivities provides an important tool to track the exsolution, mass and rate of fluid transport within long-lived shallow mushy magma reservoirs in the Earth's crust.

1. Introduction

The diffusion of trace elements in melt and crystals is a powerful chronometer for the timescales of magmatic, metamorphic, and hydrothermal processes in geological systems. Trace element diffusion can be employed as a tracer for kinetic processes, such as recharge (Shamloo and Till, 2019; Tavazzani et al., 2020; Till et al., 2015), fluid exsolution and degassing (Berlo et al., 2013; Neukampf et al., 2022; Vlastélic et al., 2013). The mobility of alkali elements is of particular interest for igneous systems, as they (1) control the electrical conductivity of silicate melts (Ni et al., 2015; Provenzano et al., 1972); (2) play an important role as flux elements (e.g. Li, Na) that increase the solubility of water and suppress the liquidus temperature in silicic melts (Maneta and Baker, 2014; Sowerby and Keppler, 2002), and (3) comprise elements of economic interest (e.g. Li, Cs) that are concentrated in granite-related ore deposits and during crystallization of pegmatites (Dill, 2015; London, 2018; O'Connor et al., 1991; Teng et al., 2006; Troch et al., 2022).

More than on any other factor, trace element diffusivities depend on temperature with elements diffusing faster with increasing temperature, as expressed by Arrhenius relationships. Trace element diffusivities in silicic melts also strongly depend on melt water contents (Watson, 1979, 1981; Zhang et al., 2010). However, the dependence of diffusivities on melt water contents is poorly understood and quantified, as most previous trace element diffusivity data were determined in water-free melts

* Corresponding author.
E-mail address: juliana.troch@pfp.rwth-aachen.de (J. Troch).

https://doi.org/10.1016/j.gca.2023.11.031
Received 27 March 2023; Accepted 29 November 2023
Available online 1 December 2023
0016-7037/© 2023 The Author(s). Published by Elsevier Ltd. This is an open access article under the CC BY-NC license (http://creativecommons.org/licenses/by-nc/4.0/).

unrealistic for most highly evolved magmatic systems.

Here, we use diffusion couple experiments to investigate the water-dependent diffusion of the alkali trace elements Li, Rb, and Cs in silicic melts with three different starting compositions: rhyodacite, high-silica rhyolite, and peralkaline rhyolite. By comparing diffusivities as a function of temperature, melt water content and composition, and ionic radius of the diffusing species, we explore the mechanisms of trace element diffusion and its dependence on the viscosity, polymerization and structure of silicate melt. We apply these results to a mechanical fluid transport model to investigate the kinetic effects caused by differential equilibration of different trace elements between fluid and melt in magmatic systems. These findings provide insights into the characteristic trace element fingerprints that various modes of fluid migration may leave in the rock record of silicic magmatic systems.

2. Methods

2.1. Starting materials and preparation

Alkali trace element diffusion parameters were obtained from diffusion couple experiments using three natural silicic starting materials of varying composition (Table 1): (1) a glassy, porphyritic sample of metaluminous to slightly peraluminous rhyodacite (Avlaki lava with alkalinity index AI = 1.00 collected from Nisyros island, Greece, labelled *Av2*), (2) a sample of crystal-free obsidian of the metaluminous to slightly peraluminous Los Posos rhyolite dome from the Valles caldera, New Mexico/USA (AI = 1.02, labelled *LPR*), and (3) a sample of glassy, crystal-free obsidian of a peralkaline rhyolite from Ascension island (labelled *Asc*). Both *LPR* and *Asc* samples were provided by the Smithsonian National Museum of Natural History (NMNH) Rock and Ore collection (samples NMNH-117464-16 for *LPR* and NMNH-113436-6 for *Asc*).

Sample *Av2* was crushed and then powdered for 4 min in a W-carbide mill at Brown University. Samples *Asc* and *LPR* were crushed in a steel cylinder on Norman Bowen's crushing station at the Earth and Planets Laboratory (EPL) of the Carnegie Institution of Science, prior to being milled for 15 min in ethanol in an agate mortar.

To produce glasses enriched in trace alkali elements, aliquots of the powders were doped with Li_2CO_3, Rb_2CO_3, and Cs_2CO_3 to result in ca. 10-20x enrichment compared to the original composition, in order to allow sufficient analytical resolution while maintaining the trace element character. The doped powders were then homogenized in ethanol in an agate mortar for 1 h. The powders were placed in a Pt crucible and melted twice in a box furnace, to remove any carbonate and allow for full homogenization. The first melting step heated the glass from 800 to 1300 °C at a rate of 5 °C/min, then holding the sample at 1300 °C for 15 min before quenching the melt by submerging the crucible bottom in a water bath. For the second melting step, samples were crushed and milled in ethanol or methanol for 30 min, and remelted in the Pt crucible for 30 min at 1300 °C. After quenching, the glass was milled again for 30 min and sieved through <100 μm mesh. Of the undoped powders, *Av2* underwent the same melting and homogenization procedure in order to melt any remaining crystals. Melting was not required for samples *LPR* and *Asc* as these are crystal-free obsidians.

2.2. Experiments

2.2.1. Homogenization experiments

The diffusion couple experiments require the synthesis of homogenous silicic glass cylinders with different water contents. $Au_{90}Pd_{10}$ capsules of 4 mm outer diameter and 18 mm length were filled with deionized water and loaded with starting powders previously dried at 110 °C for >24 h, and welded shut under Ar atmosphere using a PUK arc welder. All preparation steps were tracked by weight to account for potential mass losses or gains potentially altering the bulk water content of the experimental charge. Closed capsules were tested for leaks by submerging them in acetone for >2 h and monitoring weight changes; any capsules showing weight gain of >0.1 mg were discarded.

Homogenization experiments with 1, 2, and 4 wt% of water were conducted in Ar-pressurized rapid-quench externally-heated Mo-Hf-C-alloy (MHC) coldseal pressure vessels at ETH Zurich. The capsules were loaded into the hot end of the pressure vessel-furnace assembly, which is situated in a near-horizontal position (10° tilt, hot-side up; cf. Kueter et al., 2020). Following a pressure test at >50 MPa, the assemblage was heated to 1100 °C over an average time of 3–4 h, and then kept at 1100 °C and >150 MPa for a minimum of 30 h for complete equilibration and homogenization. Rapid quenching was achieved by tilting the vessel furnace assembly into a vertical position, resulting in the drop of the capsule from the hot end into the water-cooled cold end of the extension tube, resulting in quenching from run conditions to room temperature in less than 2 s.

Following the synthesis step, the glassy cylinders were carefully unwrapped from the metal capsule. The cylinder was cut in half with a diamond wire saw, and each half was mounted with crystal bond into a polishing stencil and polished down to 0.25 μm grainsize to produce a flat surface for optimal contact between doped and undoped glass.

Experiments with 8 wt% water required synthesis at higher pressures to allow the complete dissolution of water in the silicate glass. Glass syntheses and later diffusion experiments were performed in $Au_{90}Pd_{10}$ capsules (4 mm outer diameter × 12 mm length; same preparation as

Table 1
Normalized anhydrous major element glass compositions (via EPMA) and average trace element concentrations (via LA-ICPMS) in diffusion couple experiments.

	Av2			**LPR**			**Asc**		
	avg	±	1SD	avg	±	1SD	avg	±	1SD
SiO_2 (wt%)	71.37	±	0.65	76.76	±	0.21	73.03	±	0.31
TiO_2 (wt%)	0.30	±	0.05	0.089	±	0.020	0.20	±	0.03
Al_2O_3 (wt%)	15.03	±	0.53	12.83	±	0.16	12.91	±	0.21
FeO_{tot} (wt%)	2.25	±	0.28	0.97	±	0.10	3.16	±	0.34
MnO (wt%)	0.066	±	0.020	0.059	±	0.019	0.13	±	0.02
MgO (wt%)	0.88	±	0.07	0.025	±	0.007	<0.012	±	0.007
CaO (wt%)	2.49	±	0.34	0.35	±	0.01	0.37	±	0.02
Na_2O (wt%)	4.17	±	0.18	4.19	±	0.06	5.50	±	0.09
K_2O (wt%)	3.38	±	0.17	4.72	±	0.08	4.69	±	0.08
P_2O_5 (wt%)	0.089	±	0.023	<0.024	±	0.018	<0.024	±	0.013
A/CNK	1.00			1.02			0.87		
A/NK	1.43			1.07			0.91		
initial Li (ppmw)	33	±	1	40	±	3	25	±	1
doped Li (ppmw)	324	±	12	352	±	19	201	±	9
initial Rb (ppmw)	97	±	4	145	±	10	94	±	4
doped Rb (ppmw)	757	±	26	455	±	25	472	±	21
initial Cs (ppmw)	8.7	±	0.3	4.3	±	0.3	1.00	±	0.05
doped Cs (ppmw)	134	±	5	229	±	13	268	±	12

above) in a solid media pressure device (piston cylinder in the following (Boyd and England, 1960; Kushiro et al., 1976)). Capsules were placed into ¾-inch talc-pyrex-MgO assemblies with a tapered graphite furnace. Prior to the run, the assembly parts were heated or fired overnight at 110 and 1000 °C, respectively. The synthesis experiments were heated at 100 °C/min to 1000 °C while applying 0.7 GPa confining pressure, and kept under these conditions for 6.5 h. Experiments were quenched at a rate of 67 °C/s to about 400 °C (Kueter et al., 2021) under near-isobaric conditions by simultaneously pumping oil to maintain the piston pressure to minimize decompression cracking of the glass. Temperature was monitored and controlled with a S-type (Pt-Pt_{90}/Rh_{10}) thermocouple (without EMF pressure correction) coupled to a Watlow F4T thermocontroller. Uncertainties are ± 10 °C on the temperature and 0.1 GPa on the pressure (Mysen, 2007). Recovered capsules were cleaned from the MgO pressure medium, first mechanically using dentistry tools and then by washing them for 24 h in a magnetically stirred water bath containing 10 % HCl (heated at 70 °C) for 24 h. Capsules were subsequently cut with a diamond wire saw to remove capsule ends and produce two equally sized glass cylinders still wrapped in the metal envelope of the container to avoid glass fragmentation. One side of each cylinder was polished as outlined above.

2.2.2. Diffusion experiments

Diffusion experiments for silicate glasses with 1, 2, and 4 wt% H_2O were conducted in the same MHC coldseal pressure vessels as the homogenization experiments. For each experiment, the polished sides of a doped and undoped glass cylinder were brought in contact and loaded into a 3-mm Au capsule of 15–18 mm length, depending on the length of the respective cylinders. The capsule was welded shut with an arc welder and weighed before and after the experiment. For the experiment, the capsule was loaded into the cold end of the horizontal coldseal vessel, while the hot end was heated to the desired run temperature (see Table 2). When stable run conditions were reached (pressures >180 MPa), the vessel-furnace assembly was tilted by 90° into a vertical position, dropping the capsule into the hot end rapidly (<2 s) and exposing it to run conditions. The vessel-furnace assembly was then fixed in a near-horizontal position, and run durations were timed with a stopwatch; the exact run durations reported in Table 2 were calculated from the time between pressure signals on the monitoring screen resulting from tilting the furnace during starting and quenching of the experiment. We estimate an uncertainty of ±3 s on these run durations. Run temperatures are estimated to have an uncertainty of ±5 °C; pressure usually varied <0.4 MPa during the experiment.

Similar to above, for piston cylinder experiments polished surfaces of the 8 wt% water experiments were placed together in 5 × 10–12 mm Au containers for subsequent piston cylinder runs. To ensure close contact of the polished surfaces, the metal envelopes of the cylinders were fused together by applying a few pulsed arc welding spots at the metal contact. After preparation, the capsules underwent acetone leak testing. The experiments were conducted in the same assembly setup as outlined above. Loaded experiments were cold-compressed to 0.7 GPa and heated at 1000 °C/min to rapidly reach the desired run temperature of 720 to 950 °C (Table 2). Temperature overshooting during heating was <10 °C and persisted for <20 s. Applied runtimes were between 900 and 1320 s. Rapid, near isobaric quenching proceeded by power shut-off as outlined above. Runtimes were logged with the thermocontroller.

2.3. Analysis

2.3.1. Preparation and Laser ablation ICPMS

After the experiment, capsules were cleaned, weighed and mounted in epoxy. Experimental charges were exposed through grinding and impregnated with epoxy, before being ground and polished to expose a cross-section through the center of the experiment.

Traverses of 7 mm length were analysed across the experimental charges for the investigated trace elements Li, Rb, and Cs via a 193-nm Resonetics Resolution 155 excimer laser ablation system coupled to a Thermo Element XR sector field mass spectrometer at ETH Zurich. Additionally, we tracked all major elements as well as rare Earth elements Sm and Er to check for chemical homogeneity along the transect. For analysis, we used a rotatable 5000 × 300 μm slit, translating to a 143 × 8 μm ablation area (35x demagnification) on the sample. The slit was oriented parallel to the contact face of the two glass cylinders and rastered across the sample perpendicular to this face with a rate of 5 μm/s. Gas blanks were measured for 40 s prior to each line scan. Along the line profiles, concentrations were collected every 0.58 s, corresponding to intervals of 2.9 μm. The spatial resolution for each data point corresponds to the sum of the spatial interval (2.9 μm) and the slit width (8 μm), and thus is approximately 10.9 μm (without accounting for washout time and sequential analysis). Four evenly distributed line scans were conducted on each experimental charge. We used a pulse frequency of 10 Hz and an energy density of 3.5 J/cm^2 on the sample. Dwell times were 100 ms for Li, Rb, and Cs, and 11 ms for Na, Mg, Al, Si, P, K, Ca, Fe, Sm, and Er. Reference glass NIST 612 was analyzed with identical ablation parameters as a primary reference material after each transect on the unknown, and secondary reference glass GSD-1G was analyzed after every 6 profiles. Typical limits of detection (LOD) in this study on NIST 612 are in the range of 0.005–0.02 ppm for Li, 0.001–0.002 ppm for Rb, and <0.001 ppm for Cs, about 10 times higher for a single data point as used in the profiles. Thus all concentrations

Table 2
Experimental conditions and fitted weighted mean diffusivities (in m^2/s).

Starting material	H_2O (wt%)	Pressure (MPa)	Temp (°C)	Duration (s)	log_{10} D(Li) WM	±	2SD	log_{10} D(Rb) WM	±	2SD	log_{10} D(Cs) WM	±	2SD
Av2	0.99	186.7	806	1123	−10.005	±	0.087	−12.853	±	0.105	−13.690	±	0.108
Av2	0.99	187.4	958	600	−9.714	±	0.194	−11.947	±	0.208	−12.679	±	0.223
Av2	1.97	186.1	1100	315	−9.040	±	0.049	−11.083	±	0.046	−11.887	±	0.043
Av2	1.97	180.9	950	492	−9.407	±	0.049	−11.686	±	0.043	−12.580	±	0.042
Av2	2.01	188.0	879	608	−9.586	±	0.085	−11.929	±	0.079	−12.868	±	0.093
Av2	1.99	187.6	800	1100	−9.937	±	0.094	−12.266	±	0.150	−13.282	±	0.162
Av2	3.99	192.1	1100	315	−8.972	±	0.059	−10.489	±	0.045	−11.149	±	0.042
Av2	3.99	196.3	949	491	−9.151	±	0.058	−10.852	±	0.042	−11.608	±	0.039
Av2	3.98	194.5	1020	375	−8.974	±	0.058	−10.601	±	0.043	−11.303	±	0.039
Av2	3.98	196.9	880	615	−9.374	±	0.057	−11.313	±	0.043	−12.165	±	0.037
Av2	8.10	700.0	720	1320	−9.287	±	0.073	−10.682	±	0.092	−11.281	±	0.082
Av2	8.10	700.0	950	900	−8.941	±	0.070	−9.892	±	0.082	−10.331	±	0.080
Av2	8.00	700.0	800	1080	−9.152	±	0.095	−10.403	±	0.109	−10.959	±	0.096
Av2	8.00	700.0	880	900	−9.036	±	0.102	−10.077	±	0.114	−10.608	±	0.111
LPR	3.98	195.8	880	625	−9.288	±	0.110	−11.025	±	0.150	−11.963	±	0.093
LPR	3.98	195.0	940	500	−9.099	±	0.112	−10.647	±	0.175	−11.610	±	0.098
Asc	3.88	197.7	800	1005	−9.556	±	0.106	−11.039	±	0.114	−11.997	±	0.090
Asc	3.88	199.4	948	605	−9.077	±	0.094	−10.479	±	0.104	−11.271	±	0.076

along the diffusion profiles are at least 100 times higher than the LOD. The data were reduced using the software Iolite (https://iolite.xyz) using Al contents from electron microprobe analysis (Table 1) as internal standard element. All LA-ICPMS profile data are available in electronic suppl. S3 and plotted in S1-2.

2.3.2. Monte Carlo curve-fitting with MATLAB

The resulting profiles of Li, Rb, and Cs contents were fitted in Matlab with the classic diffusion analytical solution (Crank, 1975) for 1-D diffusion in an infinite diffusion couple with an initial step profile

$$C(x,t) = C_{min} + \mathrm{erfc}\left(\frac{x-B}{\sqrt{4\,D \bullet t}}\right) \bullet (C_{max} - C_{min}) \quad (1)$$

whereby C is the concentration of the investigated trace element at position x in m along the transect, with C_{min} being the average concentration in ppm in the undoped and C_{max} the concentration in the doped diffusion couple. B is the approximate location of the initial interface, as defined by the inflection point of the profile (usually between 3000 and 4000 μm), D is the diffusivity of the investigated trace element under conditions in the experiment, and t is the run duration of

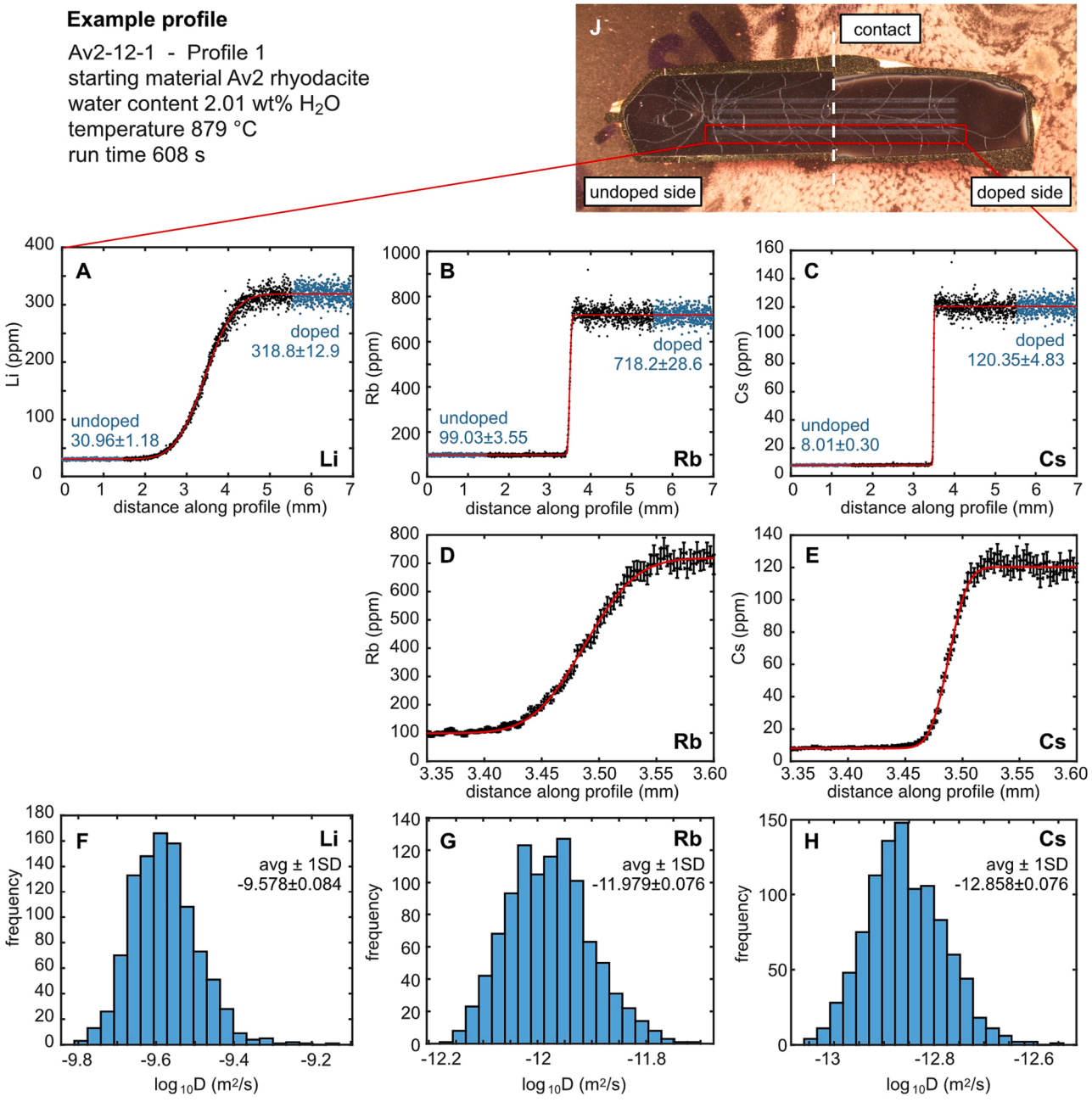

Fig. 1. Analysis and fitting procedure on example profile analyzed via LA-ICPMS from experiment Av2-12-1 at 879 °C and 2.01 wt% H_2O on a rhyodacitic melt starting composition. (A-C) Concentration gradients for Li (A), Rb (B), and Cs (C) along the same profile. For full uncertainty propagation, each of these profiles was fitted 1000 times with a Monte-Carlo approach, whereby input values for the concentrations on the doped and undoped ends and the run times were systematically varied by defining a normal distribution. For input concentrations, we use the average ± 1 standard deviation of the first and last 500 points (shown in blue) on either side of the profile. For input run times, we use the timed run durations (from Table 2) ± 3 s. (D-E) Zoomed-in profiles for Rb (D) and Cs (E). (F-H) The resulting frequency distributions are shown for Li (F), Rb (G), and Cs (H). This procedure is repeated for each of the four profiles analyzed in each experiment, with the location of the example profile shown in panel J.

the experiment in s. D and B are the parameters varied during the fitting procedure. For full error propagation, we use a Monte Carlo approach, whereby the inputs for C_{min}, $C_{max,}$ and t follow a normal distribution. For C_{max} and C_{min}, this distribution is centered around the mean trace element content on the plateau on either side of the sigmoid function determined from the first and last 500 analyses along the profile. Input for t follows a normal distribution centered around the run times given in Table 2, with a standard deviation of 3 s. Each Monte Carlo simulation includes 1000 iterations. Distribution histograms for all analysed profiles are provided in suppl. material S1-2. The code for the Matlab-based Monte Carlo fitting tool is available in suppl. material S4. Average D values for each profile are calculated based on the mean of all iterations, with the uncertainty given as 1SD (suppl. material S1-2). Final diffusivities for each experiment (Table 2) are determined from the weighted mean of the four diffusivities constrained from each profile along the experimental charge.

2.3.3. Additional EMP analyses

Major element compositions of experimental glasses and backscatter images of textures were collected using a JXA-8530FPlus HyperProbe Electron Probe Microanalyzer at the Department of Mineral Sciences at the Smithsonian National Museum of Natural History. Multiple glass analyses were obtained at 15 kV with a beam current of 10nA and diameter of 20 μm along all experimental charges, with counting times of 10 s on peak and 5 s on background for all elements, except P (20 s/10 s). All analyses and results for standard reference glasses can be found in suppl. table S2-3 and S2-4.

3. Results

3.1. LA-ICPMS profiles and experimental observations

LA-ICPMS analysis of the experimental charges reveal clear sigmoidal diffusion profiles with well-defined plateaus on both ends (Fig. 1A–E) for coldseal and piston cylinder experiments. The contacts between the diffusion couples look flat and undisturbed, and are well visible due to the slight contrast in color between the doped and undoped glass cylinders (Fig. 1J). In piston cylinder experiments, plateau length is reduced due to the shorter capsule dimensions compared to coldseal capsules, which could affect fitting of the fast-diffusing Li. We used these shorter plateau lengths as a basis for calculating the initial concentrations of the diffusive species Li, Rb, and Cs in the opposing diffusion couples for all experiments. Due to the consistency of the results for fast-diffusing Li, the reduced plateau length in the piston cylinder experiments is unlikely to have affected Li diffusion significantly.

Piston cylinder experiments at 800 and 880 °C show slight color change towards the rim of the capsule, probably due to redox reactions during the homogenization step, as this color change correlates with slight variation in Fe in the diffusion profile (Ni et al., 2021). However, the trace element profiles appear unaffected by this process. A subset of experiments was excluded after analysis of the diffusion profiles due to incomplete contact between the diffusion couples. This is apparent from the retention of the initial step profile during the diffusion experiment for all three diffusing species, illustrating how beneficial the presence of a faster-diffusing trace element (e.g. Li) is for interpreting diffusion profiles for slow-moving trace elements, such as Cs (e.g. see example A in suppl. Figs. S1-S5). Analysis of multiple profiles across the contact surface is also a useful approach for identifying experiments with partial contact between glass cylinders (e.g. example B in suppl. material S1-5). The contact area of the diffusion couples is often affected by minor cracking resulting from the decompression and relaxation of the glass during decompression after the experiment, particularly in the case of higher-pressure piston cylinder experiments. In one experiment, this resulted in the accidental removal of a crucial part of the diffusion profile during opening and polishing of the capsule. Excluded experiments are not shown in Table 2 and Fig. 2 and are not considered in the derivation of the Arrhenius parameters. H_2O contents reported in Table 2 reflect the amount of water added to the capsules prior to the homogenization experiment, as weighed during the capsule filling process. Multiple observations suggest that these are an adequate estimate for the final water content in these experiments: (1) Lack of weight loss during experimental runs as verified by repeated weighing, (2) the extremely consistent trends in diffusivities across the large number of experiments in this study, as well as literature values, and (3) the linear correlation between added water contents and water contents "by difference" as derived from EPMA totals (although these are commonly higher due to the use of anhydrous calibration materials).

3.2. Diffusivities

Measured diffusivities correlate inversely with ionic radius ($D_{Li} > D_{Rb} > D_{Cs}$), and show a strong positive correlation with temperature and water content in the experiment, with Li increasing by one order of magnitude from the driest (1 wt% H_2O) to the wettest (8 wt%) experiment (Fig. 2A), Rb more than two orders of magnitude (Fig. 2B), and Cs about 3 orders of magnitude (Fig. 2C). While heating and quenching is near-instantaneous in coldseal experiments, diffusion during heat-up and cooling could lead to overestimated diffusivities derived from piston cylinder experiments with 8 wt% H_2O. We quantify the magnitude of this effect through step-wise integration of the diffusivities along the entire temperature evolution (Suppl. S1-1 for a description of this procedure). The precise percentage by which our estimates may overestimate diffusion coefficients largely depends on the temperature below which diffusion is regarded as negligible. We use the glass transition temperature as a first-order estimate for this temperature threshold as the diffusion mechanism may differ significantly below this. Using the recorded heating and cooling ramps during the experiments, we have calculated the effect for glass transition temperatures (T_g) between 400 and 700 °C applicable to hydrous silicic melts (Giordano et al., 2005). The effect is insignificant (<0.6 %) for experiments at 720 and 800 °C, with recalculated diffusivities being within uncertainty of the stated values in Table 2 at all tested temperatures. For the 880 °C experiment, the effect only becomes significant at temperatures <500 °C, which may be unrealistic given the dependence of the glass transition on cooling/heating rates (Giordano et al., 2005) and the extremely fast heating and cooling rates used in our experiments. The effect only becomes significant in our highest-temperature piston cylinder experiment at 950 °C, where the recalculated diffusivities are between 1.05 % (for T_g at 700 °C) and 2.44 % (for T_g at 400 °C) slower than the values stated in Table 2. Due to the very small deviations (all <3 %) and the uncertainty on which temperature would be the appropriate cut-off, we do not correct the resulting diffusivities and instead refer the interested reader to suppl. Table S2-1, where this effect is assessed in detail. Temperature-diffusivity relationships for experiments at the same water content indicate near-parallel trends for Rb and Cs at different water contents (Fig. 2B–C). In contrast, trends for Li indicate a decreasing role of water for Li diffusion towards higher temperatures (Fig. 2A, D, Fig. 3). Our results compare well with Li diffusion data in the literature, e.g. diffusion data for rhyolite melt at 6 wt% H_2O from Holycross et al. (2018) falls between our data for 4 wt% and 8 wt% H_2O (Fig. 2D), and our driest experiments (1–2 wt%) sit just above diffusivities for dry rhyolite melt by Jambon and Semet (1978). Rb diffusion data for rhyolite melt with 2 wt% by Hahn et al. (2005) fall on the same trend as our data at 2 wt% H_2O (Fig. 2E). Diffusivities at 4 wt% H_2O in our experiments are similar to diffusivities at 5 wt% H_2O in andesite melt from Koepke and Behrens (2001), probably due to the more evolved compositions in our experiments. Cs diffusivities for dry rhyolite melt from Jambon (1982) and Watson (1979) compare well with the trends for hydrous melts in this study (Fig. 2F). The similarity between Cs diffusivities in our experiments at 4 wt% H_2O and those of Watson (1979) at 6 wt% H_2O may be because the earlier experiments by Watson

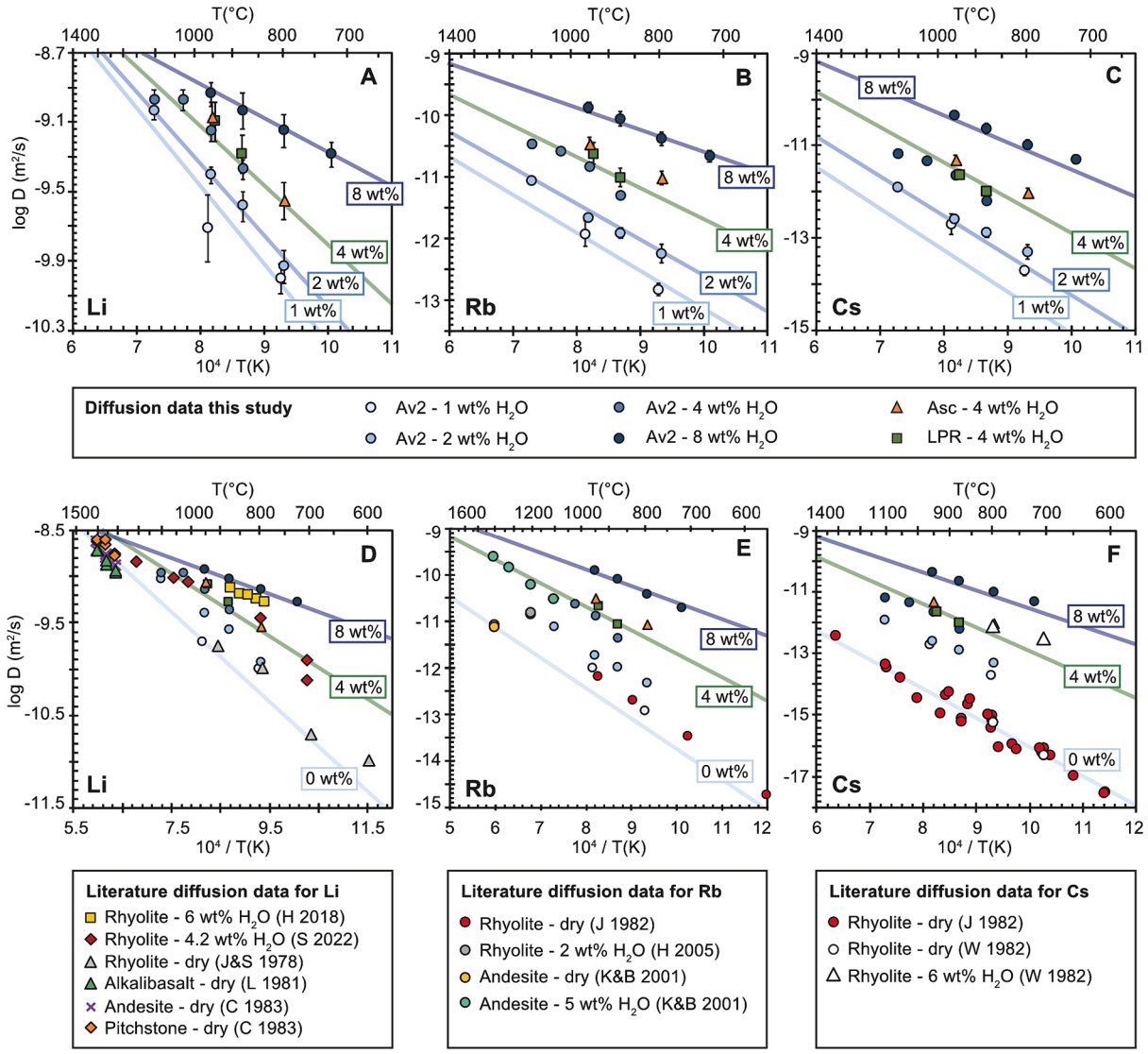

Fig. 2. (A–C) Diffusion data from this study for Li (A), Rb (B), and Cs (C) for rhyolite melt of three different starting compositions (Av2, Asc, LPR) with 1, 2, 4, and 8 wt% dissolved H_2O. Error bars show 2SD uncertainties. Trend lines in the background are modelled diffusivities for the same water contents (section 4.2), including 1SD uncertainty ranges (~0.09 log units). (D-F) Literature diffusion data for the same elements for experiments on natural melt compositions: (D) Li (Cunningham et al., 1983; Holycross et al., 2018; Jambon and Semet, 1978; Lowry et al., 1981; Spallanzani et al., 2022), (E) (Hahn et al., 2005; Koepke and Behrens, 2001), and (F) Cs (Jambon, 1982; Watson, 1979). Plots D-F also contain data from A-C without error bars for better readability. Transparent trend lines in the background are modelled diffusivities for water contents of 0, 4, and 8 wt% H_2O with 1SD uncertainty ranges (based on Eqs. (3)–(5)).

(to our knowledge the first to document the influence of water) were not conducted under confining pressure and are therefore likely to have lost some water during the experiment.

Variations in the major element composition of the rhyolite melt only have a minor effect on measured diffusivities of alkali trace elements. Diffusivities on the metaluminous to slightly peraluminous rhyolite (*LPR*) are within uncertainty of those of metaluminous to slightly peraluminous rhyodacite melt (*Av2*). Diffusivities of peralkaline rhyolite melt (*Asc*) are slightly higher for Rb, but remain close to or within the scatter of the diffusion experiments on other rhyolitic compositions (Fig. 2B).

The spatial resolution of the in situ analytical method can significantly affect diffusivity results due to convolution effects (see Jollands, 2020). We assess the scale of this effect by selecting ten profiles for Cs diffusion with a lower number of points on the slope between the high- and low-concentration ends than most other profiles, and process them with the PACE program (Program for Assessing Convolution Effects in diffusion studies, Jollands, 2020). We focus on Cs exclusively, since it is the slowest diffusion element among those studied here and therefore the one where any convolution effects would be most extreme. Assuming a spatial resolution of 10.9 μm (as derived in section 2.3.1), all deconvoluted diffusivities for these profiles are within uncertainty of those derived in our study (electr. suppl. S2-2). Even when the spatial sampling intervals are set to larger values (e.g. ≥ 15 μm, much higher than our estimated 10.9 μm), only four profiles from experiment Av2/1 wt% H_2O/806 °C/run time 1123 s would show some light convolution effects (deconvoluted diffusivities ranging from −13.93 ± 0.16 to −14.00 ± 0.19 m^2/s compared to results in this study −13.68 ± 0.12 m^2/s for the same profiles). We therefore conclude that any analytical convolution is within the stated uncertainties and does not play a significant role for the results in this study.

We use each experimental series at the different water contents to fit the Arrhenius equation

$$D = D_0 e^{\frac{-Ea}{RT}} \quad (2)$$

where D_0 is the preexponential factor in m^2/s, E_a the activation energy in

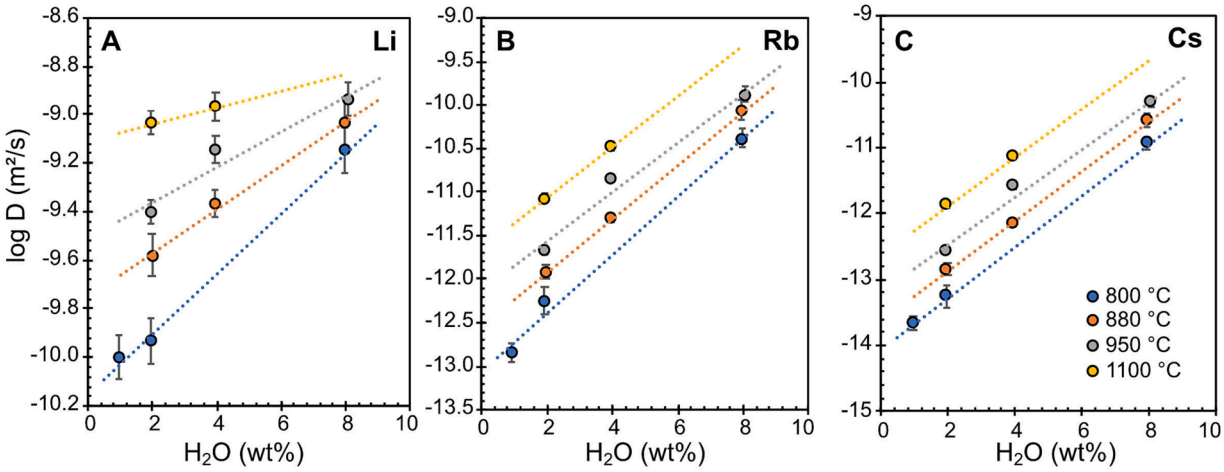

Fig. 3. Diffusivities of Li, Rb, and Cs as a function of water content in the melt at experimental temperatures of 800, 880, 950 and 1100 °C. For simplicity, this figure only shows data for experiments with starting material *Av2* and those with at least two experiments at the same temperature. Trendlines are consistent with linear dependency for all elements.

J/mol, T the temperature in K, and R the gas constant. The results for these fits are reported in Table 3, and all fits are provided in suppl. Fig. S1-3. Due to the small differences between the diffusivity results for different melt compositions, we use results from all three in order to derive the Arrhenius parameters for rhyolite melt at 4 wt% H_2O.

4. Discussion

4.1. Dependence of alkali trace element diffusion on melt water content

A strong effect of melt water contents on element diffusivities in silicate melts has been a common observation in many diffusion studies (Ni, 2012; Watson, 1979; Zhang and Ni, 2010). For neutral molecular species, it has been suggested that ln(D) and log(D) vary linearly with water content for fast-diffusing elements (Behrens and Zhang, 2001; Zhang, 2010; Zhang and Behrens, 2000), which is confirmed by our diffusion data for Li (Fig. 3A). Diffusivities for slow-diffusing elements have been suggested to more commonly depend on the square root of the water content in the melt (Zhang, 2010), however, both Rb and Cs in our experiments follow the same linear correlation as fast-diffusing Li (Fig. 3B–C).

When comparing the dependence of the Arrhenius parameters D_0 and E_a on melt water content, the preexponential factors only vary to a small degree between different H_2O contents (Fig. 4), although the uncertainties are considerable given the multiple fitting steps required for this fit. On the other hand, the activation energies show a strong negative linear correlation with melt water contents, in agreement with other studies (e.g. Spallanzani et al., 2022). If we assume that a crossover of diffusivities occurs at very high temperatures (i.e. 1400–1500 °C for Li, Fig. 2), then D_0 must also vary as a function of H_2O, in order to counterbalance the effect of H_2O on E_a (and thus on the slope in the Arrhenius diagram).

Diffusivities are commonly linked back to melt viscosities, e.g. by comparison with Eyring diffusivities (Chakraborty, 1995; Mungall, 2002; Spallanzani et al., 2022). Both diffusivities and melt viscosities result from the melt structure (controlled by melt composition, water content, temperature and pressure) and therefore correlate closely, but are not mutually dependent (Fig. 5). As the more easily quantifiable parameter, viscosity models (e.g. Giordano et al., 2008) often provide a more carefully tuned description of the melt configuration than simplified expressions for melt polymerization, such as NBO/T, which rarely account for H_2O (e.g. Mills et al., 2014).

Diffusivities of all melt components increase with increasing dissolved water in the melt. Water effectively dissociates a polymerized silicate network through the reaction Si—O—Si + H_2O → 2 SiOH, increasing the amount of unbonded silicate tetrahedra with hydrogen-terminated non-bridging oxygens (silanols) (Maekawa et al., 1998; Zotov and Keppler, 1998) and thus reducing polymerization. Such a decreasingly connected tetrahedral network statistically provides more pathways for diffusion, both for network-forming Si units (or rather SiO_4 or Q^n species) as well as for alkali elements that are closely associated with Si-Al-complexes via charge balance.

Diffusion of network-modifying alkali elements is thought to be decoupled from the silicate matrix and to proceed faster than that of network formers, such as Si, Al, and O (Angell, 1988; Dingwell, 1990; Mysen et al., 1982). Notably, diffusivities for smaller interstitial ions, such as Li, closely follow viscosities and merge on a single trend independent of the experimental temperature (Fig. 5). In contrast, trends for the larger Rb and Cs ions differ depending on the experimental temperature, indicating stronger steric and electrostatic interaction of large-radii alkalis with the tetrahedral melt network. Stronger coupling is

Table 3
Arrhenius fit parameters with 95 % confidence intervals for experiments with different water contents.

Sample	H_2O (wt %)	$\log_{10}D_0$ (m^2/s)	±	2SD	E_a (kJ/mol)	±	2SD
Lithium							
Av2	0.99	−7.65	±	1.07	48.7	±	22.9
Av2	1.99	−5.94	±	0.78	81.3	±	18.6
Av2	3.99	−6.70	±	0.97	58.1	±	23.2
Av2	8.05	−7.45	±	1.02	35.0	±	21.4
LPR	3.98	−5.42	±	2.15	85.4	±	48.7
Asc	3.88	−5.61	±	0.75	81.1	±	16.5
all	3.96	−6.70	±	0.45	57.9	±	10.6
Rubidium							
Av2	0.99	−5.50	±	1.19	151.9	±	25.6
Av2	1.99	−6.59	±	0.85	118.5	±	20.5
Av2	3.99	−6.03	±	0.73	114.9	±	17.5
Av2	8.05	−6.43	±	1.22	81.0	±	25.9
LPR	3.98	−3.31	±	3.16	170.4	±	71.5
Asc	3.88	−6.41	±	0.82	95.1	±	18.0
all	3.96	−6.78	±	0.37	96.0	±	8.8
Cesium							
Av2	0.99	−5.50	±	1.26	169.3	±	27.0
Av2	1.99	−6.60	±	0.85	139.3	±	20.6
Av2	3.99	−5.60	±	0.65	143.0	±	15.5
Av2	8.05	−6.23	±	1.15	96.4	±	24.1
LPR	3.98	−4.75	±	1.86	159.2	±	42.1
Asc	3.88	−6.01	±	0.62	123.0	±	13.7
all	3.96	−6.41	±	0.32	122.7	±	7.6

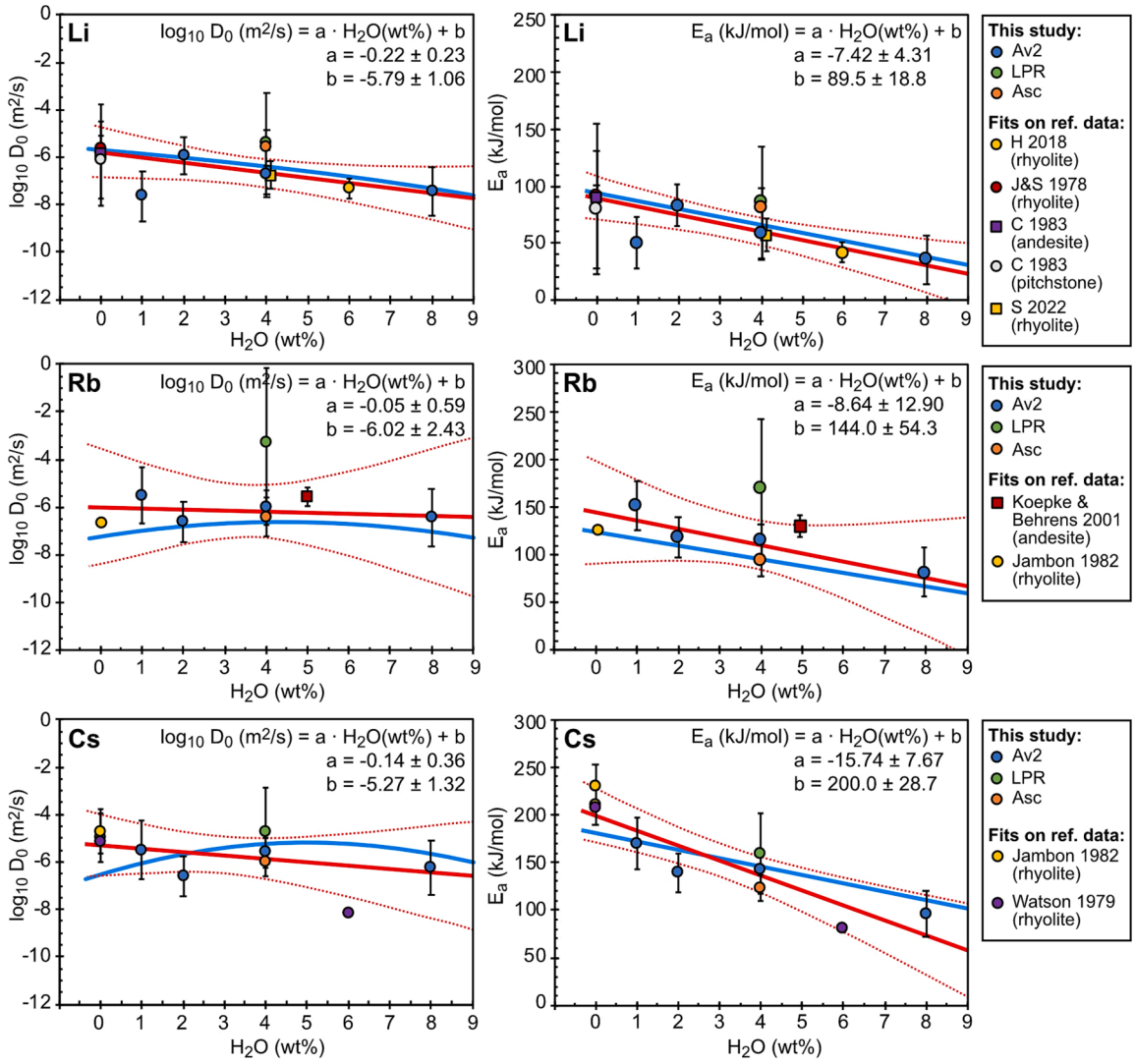

Fig. 4. Preexponential factors (left panels) and activation energies (right panels) from fits in Table 3 as a function of water content, including fitted log D_0 and Ea values based on literature data for Li (Cunningham et al., 1983; Holycross et al., 2018; Jambon and Semet, 1978; Spallanzani et al., 2022), Rb (Jambon, 1982; Koepke and Behrens, 2001) and Cs (Jambon, 1982; Watson, 1979). Expressions with 95% confidence intervals (red lines) are based on linear fits of all rhyolite data (both this study and literature data) that include uncertainty estimates (i.e. leaving out Li and Rb data on andesite, and Cs data from Watson (1979). We do not consider Rb diffusion data from Hahn et al. (2005) in these fits, as their experiments were all conducted at the same temperature and therefore do not allow fitting of Arrhenius parameters. Blue lines show $\log_{10}D_0$ and E_a values from Eqs. (6)–(11) based on modelled diffusivities from Eqs. (3)–(5) (see text for details on how these are derived). Note that the large uncertainties and slight offset of fitted parameters on the LPR starting material are an artefact resulting from the low number of experiments (2) and the slightly higher slope between their diffusivity estimates in Fig. 2.

consistent with the more pronounced compositional dependence of diffusivities for Rb and Cs compared to Li (Fig. 2), although generally, the effect of varying anhydrous melt compositions on diffusivities is small when compared to the effects of changing temperatures or water contents (Fig. 2). The solvation of alkali ions in the silicate network proceeds primarily via dipole bonding to non-bridging oxygens (NBO). Due to the increase in electronegativity with ionic radius, larger-radii alkalis are associated with stronger bonding and clustering of OH-groups (or silanols) (Kueter et al., 2021; Le Losq et al., 2016; Le Losq et al., 2015). For these elements, it is possible that such alkali-NBO configurations are therefore less mobile, reducing their effective diffusive flux.

When comparing diffusivities of the different elements, log$D$ values decrease with increasing ionic radius and decreasing ionic field strength (Z/r^2). Based on the curvature of this trend (already noted by Roselieb and Jambon (1997) and references within), Mungall (2002) proposed in his empirical diffusivity model that instead of just the ionic radius, diffusivities varied more closely as a function of the factor $(r - d)^2$, which is the difference between the ionic radius r (in Å) of the diffusing element and the doorway radius d (in Å), a critical radius threshold describing the permeability of the melt network. The idea in this model is that the closer the cation radius is to the doorway radius, the smaller $(r - d)^2$ will be, and the less energy will be required for cations to move through the melt network. When comparing diffusivities of Li, Rb, and Cs at the same temperatures and water contents, we find that indeed diffusivities can be expressed with an inverse parabola (Fig. 6). However, this would mean that elements with a smaller ionic radius than Li would be predicted to have lower diffusivities, which is not realistic given that e.g. hydrogen diffuses over similar timescales as Li in dry silicic melts (Fig. 6, Zhang and Ni, 2010; Zhang et al., 2010). We therefore do not believe that the doorway radius concept is applicable to trace element diffusion.

Water contents in silicic melts are restricted by water solubility limits, leading to the exsolution of an aqueous fluid phase if the water content in the system exceeds the water solubility in the melt as predicted by solubility models (Liu et al., 2005; Newman and Lowenstern, 2002; Papale et al., 2006). The observation that (1) the slope in the

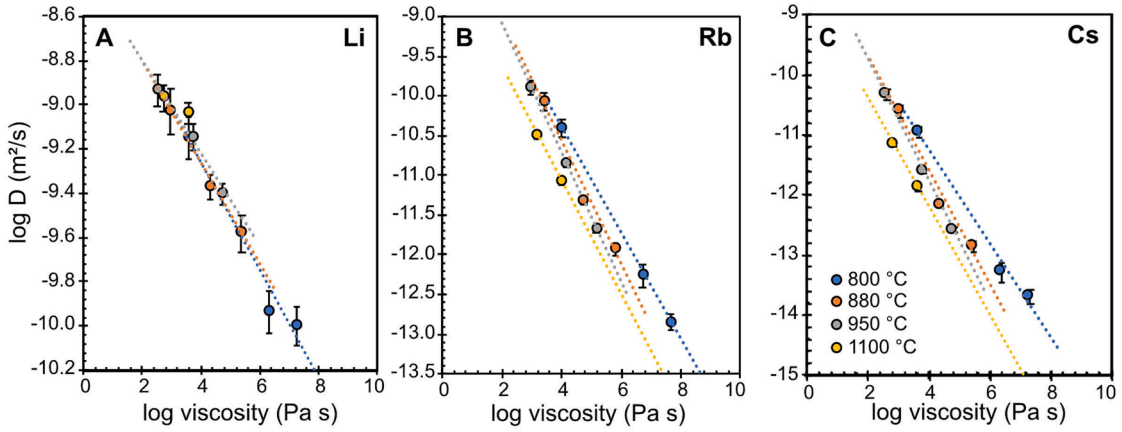

Fig. 5. Diffusivities of Li, Rb, and Cs as a function of viscosities calculated after (Giordano et al., 2008). For simplicity, this figure only shows data for experiments with starting material *Av2* and those with at least two experiments at the same temperature (i.e. same set of experiments as in Fig. 3).

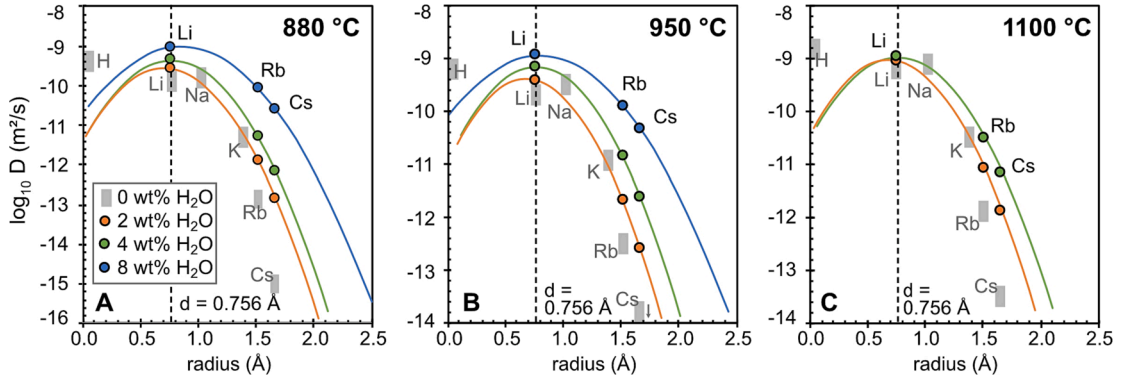

Fig. 6. (A–C) Diffusivities as a function of ionic radius (Shannon, 1976, assuming 6-fold coordination) at different temperatures and water contents. The average radius at maximum diffusivity gives a higher doorway radius estimate (d = 0.756 Å) compared to the estimate used by Mungall (2002). Diffusivities for H, Na, and K are based on Jambon (1982), Magaritz and Hofmann (1978), Van der Laan et al. (1994), Watson (1981), Zhang and Ni (2010). Note that diffusion mechanisms for H are complex and may differ fundamentally from alkali elements; we only include hydrogen here to illustrate the shortfalls of the doorway radius concept. At 1100 °C, we did not conduct an experiment with 8 wt% H_2O, as the required short run duration would have meant that diffusivity results (particularly for Li) would have been heavily controlled by diffusion during heating and cooling of the piston cylinder experiment.

Arrhenius diagram (i.e. E_a) depends on melt water contents (Figs. 2, 4), (2) diffusivities of fast-diffusing Li converge at high temperatures (Fig. 2), and (3) the effect of water on diffusivities at a given temperature apparently decreases for ions with smaller radii (Fig. 6) all indicate that trace element diffusivities in silicic melts level out at high temperatures and water contents, and are essentially capped by a maximum diffusivity limit (Fig. 7). At geologically relevant temperatures and water solubility values in the Earth's crust, this diffusivity limit will rarely apply, and only small-radius elements (e.g. Li, H) in exceptional circumstances may come close to reaching the maximum diffusivity (Fig. 7). However, this effect could play a role for fast-diffusing species in deep and hydrous high-temperature melts derived from the mantle. It may also explain some of the observed discrepancies in the diffusivity-water relationships for different elements (Zhang, 2010), such as the discussion whether diffusivities vary linearly with water contents or with the square root of water contents.

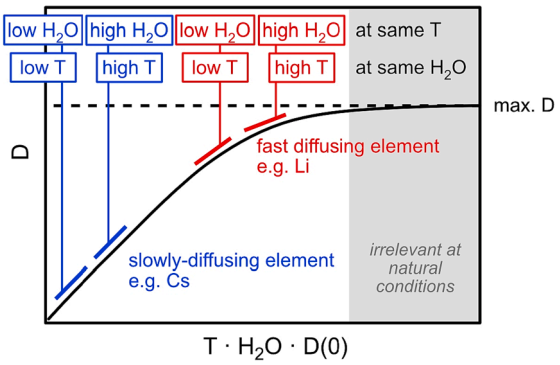

Fig. 7. Schematic diagram illustrating the different T and H_2O dependencies of diffusivities for fast-diffusing and slowly-diffusing elements respectively. D(0) here refers to the diffusivity at T = ∞ and 0 wt% H_2O, corresponding to the pre-exponential factor in dry melts. The concept of a maximum attainable diffusivity could explain the variable slopes for fast-diffusing elements (such as Li) at different melt water contents in the Arrhenius diagram (Fig. 2), as well as in logD vs. H_2O space for different temperatures (Fig. 3). At the same conditions, $\partial D/\partial T$ and $\partial D/\partial H_2O$ remain constant for more slowly diffusing elements, such as Cs.

4.2. A predictive model for H_2O-dependent trace element diffusion

Several studies have developed empirical models for predicting alkali trace element diffusivities as a function of melt compositional parameters, e.g. most commonly as a function of Na, K, Al and Ca contents and the ratio of network-forming and network-modifying elements in the melt (Mungall, 2002; Ni, 2012; Zhang and Ni, 2010). Due to a lack of systematic data acquired on water-bearing systems, however, these

models could not account for the effect of water. In the following, we develop empirical expressions for diffusivities of alkali trace elements as a function of H_2O in average rhyolitic melts. We neglect any compositional or pressure effects here due to their limited role compared to temperature and water contents.

We can express our diffusivity results (in m^2/s) as a function of temperature (in K) and melt water content H_2O (in wt%) with the following polynomial relationships:

$$\log D_{Li} = -5.728 - 0.4859\frac{10^4}{T(K)} - 0.1367 H_2O + 0.03645\frac{10^4 H_2O}{T(K)} - 0.007918 H_2O^2 \quad (3)$$

$$(\text{with } R^2 = 0.9928 \text{ and uncertainty of } \pm 0.035 \text{ log units 2SD on fit})$$

$$\log D_{Rb} = -7.198 - 0.6541\frac{10^4}{T(K)} + 0.2569 H_2O + 0.03741\frac{10^4 H_2O}{T(K)} - 0.02974 H_2O^2 \quad (4)$$

$$\left(\text{with } R^2 = 0.9909 \text{ and uncertainty of } \pm 0.24 \text{ log units 2SD on fit}\right)$$

$$\log D_{Cs} = -6.554 - 0.9453\frac{10^4}{T(K)} + 0.5463 H_2O + 0.0449\frac{10^4 H_2O}{T(K)} - 0.05415 H_2O^2 \quad (5)$$

$$\left(\text{with } R^2 = 0.973 \text{ and uncertainty of } \pm 0.62 \text{ log units 2SD on fit}\right)$$

Note that despite the linear dependence of log$D$ values on water contents and 1/T values, these fits require a second-order form for H_2O to adequately capture the change in slope of temperature trends in the Arrhenius diagram at varying melt water contents (Fig. 2), or the different slopes of the linear trends between log$D$ values and H_2O contents at different temperatures (Fig. 3).

Due to the numerous fitting steps involved in the above procedure, we abstain from conducting a full error propagation and instead quantify the uncertainty from comparison with the experimental data by iteratively increasing the uncertainty of our model estimates in 0.001 log unit intervals until >95 % (2 sigma) of our modelled log$D$ estimates fall within the 2SD range of the experimentally determined diffusivities. Note that the resulting uncertainties (cited next to Eqs. (3)–(5), and additionally provided for the individual parameters in suppl. file S1-4) are uncertainties of the fit only; for this reason fit uncertainties are small for Li (where uncertainty on the experimentally-derived diffusivities are large relative to the diffusivity estimates) compared to Cs (where experimental uncertainties are small relative to Cs diffusivities). If we treat experimental data (this study only) and modelled diffusivities (including literature reference data) as uncorrelated entities, we can derive general average 2SD uncertainties on the above expressions of ±0.011 log units for Li, ±0.031 log units for Rb, and ±0.074 log units for Cs.

Alternatively, the diffusivities in Eqs. (3)–(5) can be described in terms of the Arrhenius parameters logD_0 (in m/s^2) and E_a (in kJ/mol) with the following equations (also shown as blue lines in Fig. 4, with 95 % confidence bounds provided in suppl. file S1-4):

$$\log D_0(\text{Li}) = -0.007918\,H_2O^2 - 0.1367\,H_2O - 5.728 \quad (6)$$

$$E_a(\text{Li}) = -6.978\,H_2O + 93.02 \quad (7)$$

$$\log D_0(\text{Rb}) = -0.02974\,H_2O^2 + 0.2569\,H_2O - 7.198 \quad (8)$$

$$E_a(\text{Rb}) = -7.162\,H_2O + 125.2 \quad (9)$$

$$\log D_0(\text{Cs}) = -0.05415\,H_2O^2 + 0.5463\,H_2O - 6.554 \quad (10)$$

$$E_a(\text{Cs}) = -8.596\,H_2O + 181.0 \quad (11)$$

Even though the calibration data set for the diffusivity expressions above (Eqs. (3)–(11)) includes some data at low temperatures, we recommend using them only in the temperature range where water-bearing experiments were conducted (~700–1100 °C), as no water-bearing experiments are currently available for temperatures <700 °C.

4.3. Differential diffusion as a tool to track fluid transport

Between any two phases, elements with higher diffusivities equilibrate over shorter timescales than elements with lower diffusivities. Kinetic effects, whereby elements equilibrate incompletely, are particularly likely when elements in these two phases have vastly different diffusivities, e.g. fast elemental transport in a magmatic volatile phase (MVP, describing broadly any aqueous fluid, gas or supercritical fluid) compared to slower elemental transport in silicic melt. In this case, the slowest diffusivity is the limiting factor during progressive equilibration between melt and MVP.

In order to illustrate the effect of differences in water-dependent diffusivities in silicic melts on trace element budgets in silicic magmatic systems, we apply our data to the fluid transport and metal extraction model by Huber et al. (2012). This model considers the advection of MVP in a permeable crystal mush and the partitioning of trace elements between rhyolite melt and MVP trapped in the pore space. Here, we assume a steady-state scenario (e.g. steady-state degassing) whereby the top of the mush section does not evolve chemically over time and reaches a balance between transport and local equilibration by diffusion.

The model includes expressions for the distribution of variably fluid-mobile elements between the MVP and melt as a function of the Péclet number (*Pe*), which expresses the ratio of advection to diffusive equilibration in the system as

$$Pe = \frac{U_g(\delta - R)^2}{MD_iH} \quad (12)$$

where U_g is the velocity of MVP in the pore space (in m/s), δ-R is the average melt-fluid diffusion path length (or the melt thickness around the fluid channel in m, here taken to be around 200 μm), H is the height of the overlying mush (in m), and M is the mass ratio of MVP and melt in the system (~0.04 for crystallinities between 50 and 70 % and MVP pore volume fractions of 20 % required to form continuous MVP channels (Huber et al., 2012)). At low *Pe*, diffusion in the melt is much faster than MVP advection through the system, resulting in trace element concentrations controlled by equilibrium partition coefficients K. At high *Pe*, trace element concentrations in both MVP and melt are controlled by the extent of possible equilibration with the melt and thus by trace element diffusivities. The observed trace element distributions between MVP and

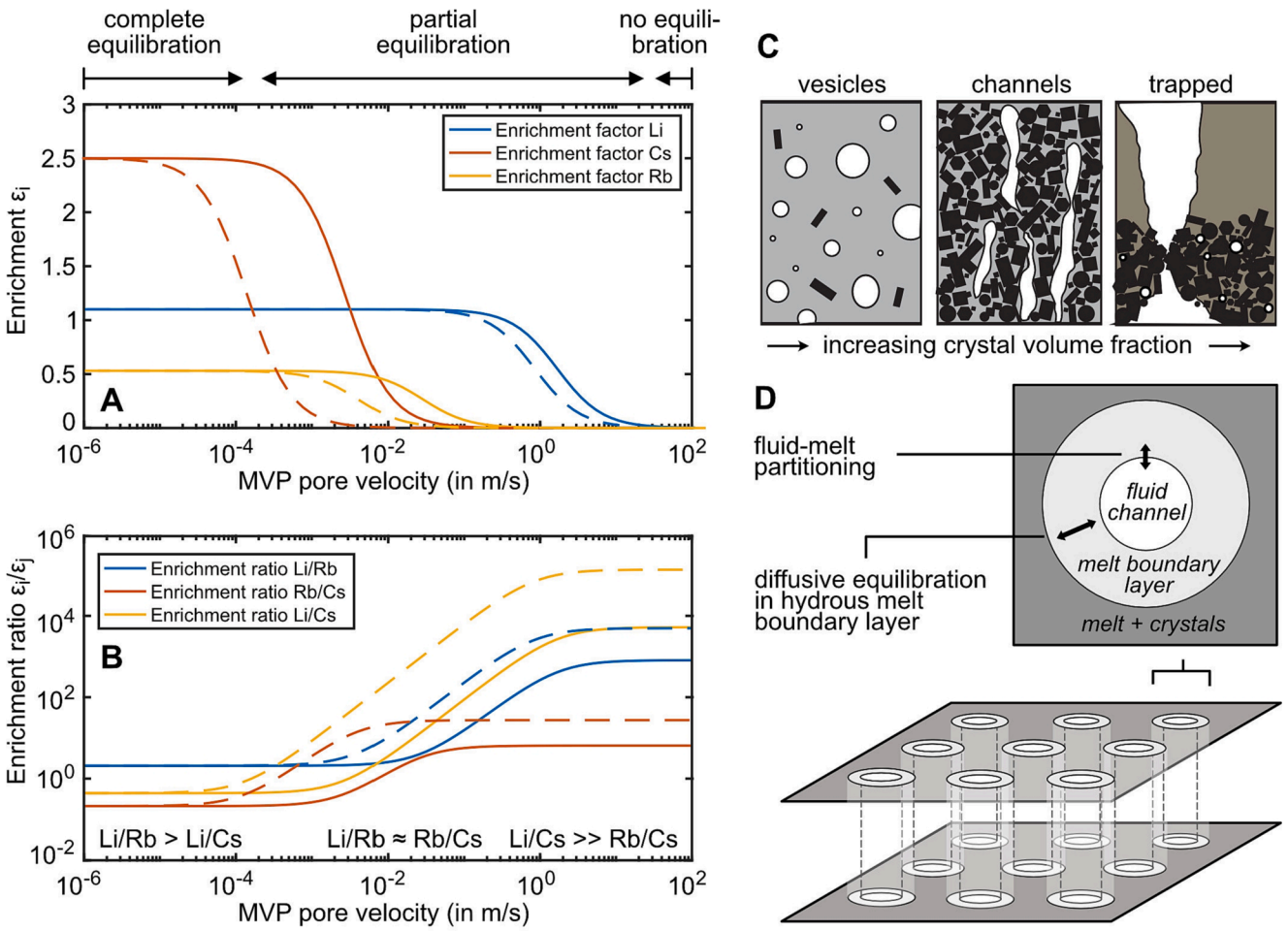

Fig. 8. (A) Modelled element enrichment in MVP compared to melt for Li, Rb, and Cs based on diffusivities in this study at 800 °C and 4 wt% (solid lines) and 2 wt% melt water content (dashed lines) in a mushy silicic system with a mush thickness of 1000 m. (B) Ratio of enrichment factors shown in A from the same model. (C) At intermediate crystal volume fractions, MVP transport predominantly occurs in channels. (D) Schematic setup for model in A + B based on Huber et al. (2012).

melt (enrichment factor ε, Eqs. (10) and (12b) in Huber et al. (2012) are defined as

$$\varepsilon_i = \frac{C_i^f}{C_i^m} = \varepsilon_i^0 - \frac{\varepsilon_i^0 - K_i}{1 + (0.165 Pe_i)^{1.456}} \quad (13)$$

where C_i^f and C_i^m are the concentrations of an element i in the fluid and melt, respectively, ε_i^0 is the initial enrichment factor of element i and refers to the concentration ratio between MVP and melt at the bottom of a mush layer. The enrichment factor ε_i essentially describes the *observed* partitioning of a trace element i between MVP and melt, and is not to be confused with K_i, which is the *equilibrium* partition coefficient of that element between MVP and melt.

To illustrate the effect on alkali trace element budgets in silicic magmatic systems, we calculate the enrichment of Li, Rb, and Cs in a mushy silicic magmatic system (50–70 % crystal volume fraction at 800 °C, 4 wt% dissolved H_2O in melt) of a thickness of 1000 m (Fig. 8). For extremely high MVP transport rates ($Pe \rightarrow \infty$), the enrichment factor approaches ε^0 or zero for initially low-solute fluids ($\varepsilon^0 \sim 0$, as shown in Fig. 8A). At low MVP velocities ($U_g < 10^{-5}$ m/s for a system with 2 wt% dissolved H_2O in the melt or $U_g < 10^{-3}$ m/s for a system with 4 wt% dissolved H_2O in example in Fig. 8A), the enrichment factor is dominantly controlled by the equilibrium partitioning behavior between fluid and melt. The ratios of alkali enrichment factors (Fig. 8B) are similarly controlled by equilibrium partition coefficients at low MVP transport rates. At high MVP transport rates ($U_g > 5$ m/s for a system with 2 wt% dissolved H_2O in the melt or $U_g > 10$ m/s for a system with 4 wt% dissolved H_2O, Fig. 8B), this ratio is effectively governed by the relative diffusivity contrast for these elements. This effect makes the ratio of enrichment factors a particularly suitable indicator for the average MVP transport rate and the extent of fluid-melt equilibration in the system, with ε(Li)/ε(Rb) > ε(Li)/ε(Cs) indicating near complete equilibration between MVP and melt at low advection rates, ε(Li)/ε(Rb) ≈ ε(Rb)/ε(Cs) suggesting partial equilibration at intermediate MVP advection rates, and ε(Li)/ε(Cs) ≫ ε(Rb)/ε(Cs) indicating incomplete equilibration when the system is intensely flushed with MVP (Fig. 8B).

Unfortunately, quantifying trace elements in co-existing fluid and melt inclusions is notoriously difficult, as illustrated by the range of published fluid/melt partition coefficients derived from natural samples (Fiedrich et al., 2020; Zajacz et al., 2008). Direct comparisons with natural inclusion assemblages are complicated by the various assumptions that must be made about starting concentrations, equilibrium partition coefficients, and fluid/melt ratios within the system. Nevertheless, detailed trace element geochemistry linked to coupled physicochemical models has the potential to become a valuable tool for tracking MVP transport in the future, particularly when based on partition and diffusion coefficients derived simultaneously for a group of trace elements from the same experiments.

5. Conclusions

Our diffusion couple experiments show that alkali trace element diffusion in silicic melts is strongly dependent on melt water content, with one order of magnitude increase for Li, two orders for Rb and three

orders for Cs from driest (1 wt%) to wettest (8 wt%) experiment. The increase in diffusivity is driven by water-related increasing depolymerization of the melt structure, with Rb and Cs showing stronger coupling with the melt than predicted from changes in viscosity alone. The crossover of diffusivities of the fastest diffusing species at high temperatures suggests that diffusivities level out at high H_2O contents, following a sigmoidal function in $\log_{10}D$ vs. $D_0 \cdot H_2O \cdot T$ space. This relationship explains the observed linear trends of Li, Rb, and Cs diffusivities with melt water contents in our experiments, while also elucidating discussions on whether diffusivities depend linearly on H_2O or its square root.

The timing, rate and mechanisms of fluid exsolution are essential parameters in understanding the long-term dynamics of magma storage and eruption. Quantifying the effects of variable melt water contents facilitates using the diffusion of alkali trace elements for tracking fluid transport, as illustrated by a two-phase mechanical model for channelized fluid flow in a mushy silicic magma reservoir. In particular, ratios of enrichment in the fluid over melt (i.e. enrichment factors) for elements of varying diffusivities may provide a powerful tool to derive rates of fluid transport in long-lived shallow mushy magma reservoirs in the Earth's crust.

Data availability

Research data has been supplied via a repository: https://doi.org/10.17632/cfdzx2rh8z.1.

Declaration of competing interest

The authors declare that they have no known competing financial interests or personal relationships that could have appeared to influence the work reported in this paper.

Acknowledgements

This paper is dedicated to Jim Webster (AMNH), who designed the initial experimental study in collaboration with CH and OB, but sadly was unable to see its beginning, and Mac Rutherford (Brown), who helped with multiple trial runs. We are very grateful to Steve Parman for lab access and support with preliminary experiments for this study at Brown University, and Soumen Mallick and Joe Boesenberg for their help in characterizing starting materials. Paul Petschnig, Manuel Pimenta Silva, and Gino Sartori are thanked for their help and upkeep of the coldseal experimental lab at ETH, Pete Tollan for his help with LA-ICPMS analyses, and Julian Hübner at RWTH for helping with sample preparation. We thank Leslie Hale from the NMNH Rock and Ore collection for providing the *Asc* starting material, and Nick Tailby and Keiji Hammond from AMNH for kindly sharing their *LPR* starting material and this journey. This study was supported by National Science Foundation grant no. EAR 1760004, covering JT and CH, Swiss National Science Foundation grant no. 200021_178928 covering JT and OB, and Swiss National Science Foundation grant no. 200020_184867 covering PU. JT was further funded by a Peter Buck postdoctoral fellowship at NMNH, and NK by a Carnegie postdoctoral fellowship.

Appendix A. Supplementary material

Supplementary material S1 (pdf file): *S1-1:* Full-length diffusion profiles of Li, Rb, Cs for all experimental runs, including the average fit and frequency diagrams of the Monte Carlo fitting procedure. *S1-2:* Arrhenius fits obtained for experiments at each water content. *S1-3:* Fitting parameters obtained for the expressions of diffusivities, pre-exponential factors and activation energies (Eqns. 3-11). *S1-4:* Two examples of incomplete contact of diffusion couple glass cylinders and the effect on diffusion profiles. **Supplementary material S2 (Excel file):** *S2-1:* Assessment of the effect of heating and cooling ramps on the diffusivity results from piston cylinder experiments. *S2-2:* Convolution assessment of 13 Cs diffusion profiles via PACE. *S2-3:* Electron microprobe analyses of glass compositions in diffusion experiments. *S2-4:* Electron microprobe analyses of standard reference glasses analysed during the same session as experimental glasses. *S2-5:* Compilation of diffusion data used for the calibration of the diffusion expressions (Eqns. 3-5). **Supplementary material S3 (Excel file):** *S3:* Data of all diffusion profiles in this study as analyzed by LA-ICPMS. **Supplementary material S4 (zip file):** *S4:* Matlab code (.m) for the Monte Carlo fitting tool (zip-file). Supplementary material to this article can be found online at https://doi.org/10.1016/j.gca.2023.11.031.

References

Angell, C.A., 1988. Structural instability and relaxation in liquid and glassy phases near the fragile liquid limit. J. Non Cryst. Solids 102 (1–3), 205–221.
Behrens, H., Zhang, Y., 2001. Ar diffusion in hydrous silicic melts: implications for volatile diffusion mechanisms and fractionation. Earth Planet. Sci. Lett. 192 (3), 363–376.
Berlo, K., Tuffen, H., Smith, V., Castro, J., Pyle, D., Mather, T., Geraki, K., 2013. Element variations in rhyolitic magma resulting from gas transport. Geochim. Cosmochim. Acta 121, 436–451.
Boyd, F., England, J., 1960. Apparatus for phase-equilibrium measurements at pressures up to 50 kilobars and temperatures up to 1750° C. J. Geophys. Res. 65 (2), 741–748.
Chakraborty, S., 1995. Diffusion in silicate melts. In: Stebbins, J.F.M., Paul F; Dingwell, Donald B. (Ed.) Structure, Dynamics, and Properties of Silicate Melts. De Gruyter, pp. 411-504.
Crank, J., 1975. The Mathematics of Diffusion, 2nd ed. Oxford University Press.
Cunningham, G., Henderson, P., Lowry, R., Nolan, J., Reed, S., Long, J., 1983. Lithium diffusion in silicate melts. Earth Planet. Sci. Lett. 65 (1), 203–205.
Dill, H.G., 2015. Pegmatites and aplites: their genetic and applied ore geology. Ore Geol. Rev. 69, 417–561.
Dingwell, D.B., 1990. Effects of structural relaxation on cationic tracer diffusion in silicate melts. Chem. Geol. 82, 209–216.
Fiedrich, A.M., Laurent, O., Heinrich, C.A., Bachmann, O., 2020. Melt and fluid evolution in an upper-crustal magma reservoir, preserved by inclusions in juvenile clasts from the Kos Plateau Tuff, Aegean Arc, Greece. Geochim. Cosmochim. Acta.
Giordano, D., Nichols, A.R., Dingwell, D.B., 2005. Glass transition temperatures of natural hydrous melts: a relationship with shear viscosity and implications for the welding process. J. Volcanol. Geoth. Res. 142 (1–2), 105–118.
Giordano, D., Russell, J.K., Dingwell, D.B., 2008. Viscosity of magmatic liquids: a model. Earth Planet. Sci. Lett. 271 (1–4), 123–134.
Hahn, M., Behrens, H., Tegge-Schüring, A., Koepke, J.R., Horn, I., Rickers, K., Falkenberg, G., Wiedenbeck, M., 2005. Trace element diffusion in rhyolitic melts: comparison between synchrotron radiation X-ray fluorescence microanalysis (μ-SRXRF) and secondary ion mass spectrometry (SIMS). Eur. J. Mineral. 17 (2), 233–242.
Holycross, M., Watson, E., Richter, F., Villeneuve, J., 2018. Diffusive fractionation of Li isotopes in wet, highly silicic melts. Geochem. Perspectives Lett. 6, 39–42.
Huber, C., Bachmann, O., Vigneresse, J.L., Dufek, J., Parmigiani, A., 2012. A physical model for metal extraction and transport in shallow magmatic systems. Geochem. Geophys. Geosyst. 13 (8).
Jambon, A., 1982. Tracer diffusion in granitic melts: experimental results for Na, K, Rb, Cs, Ca, Sr, Ba, Ce, Eu to 1300 C and a model of calculation. J. Geophys. Res. Solid Earth 87 (B13), 10797–10810.
Jambon, A., Semet, M.P., 1978. Lithium diffusion in silicate glasses of albite, orthoclase, and obsidian composition: an ion-microprobe determination. Earth Planet. Sci. Lett. 37 (3), 445–450.
Jollands, M.C., 2020. Assessing analytical convolution effects in diffusion studies: applications to experimental and natural diffusion profiles. PLoS One 15 (11), e0241788.
Koepke, J., Behrens, H., 2001. Trace element diffusion in andesitic melts: an application of synchrotron X-ray fluorescence analysis. Geochim. Cosmochim. Acta 65 (9), 1481–1498.
Kueter, N., Schmidt, M.W., Lilley, M.D., Bernasconi, S.M., 2020. Kinetic carbon isotope fractionation links graphite and diamond precipitation to reduced fluid sources. Earth Planet. Sci. Lett. 529, 115848.
Kueter, N., Cody, G.D., Foustoukos, D.I., Mysen, B.O., 2021. Hydrogen isotope fractionation inside silicate melts and glasses studied by ^{1}H and ^{2}H MAS NMR spectroscopy–Molecular insights into deuterium exchange at the melt-fluid interface. Geochim. Cosmochim. Acta 309, 171–190.
Kushiro, I., Yoder Jr, H., Mysen, B., 1976. Viscosities of basalt and andesite melts at high pressures. J. Geophys. Res. 81 (35), 6351–6356.
Le Losq, C., Mysen, B.O., Cody, G.D., 2015. Water and magmas: insights about the water solution mechanisms in alkali silicate melts from infrared, Raman, and 29 Si solid-state NMR spectroscopies. Prog Earth Planet Sci 2 (1), 1–16.
Le Losq, C., Mysen, B., Cody, G., 2016. Intramolecular fractionation of hydrogen isotopes in silicate quenched melts. Geochem. Perspect. Lett 2, 87–94.
Liu, Y., Zhang, Y., Behrens, H., 2005. Solubility of H_2O in rhyolitic melts at low pressures and a new empirical model for mixed H_2O–CO_2 solubility in rhyolitic melts. J. Volcanol. Geoth. Res. 143 (1–3), 219–235.

London, D., 2018. Ore-forming processes within granitic pegmatites. Ore Geol. Rev. 101, 349–383.
Lowry, R., Reed, S., Nolan, J., Henderson, P., Long, J., 1981. Lithium tracer-diffusion in an alkali-basaltic melt—An ion-microprobe determination. Earth Planet. Sci. Lett. 53 (1), 36–40.
Maekawa, H., Saito, T., Yokokawa, T., 1998. Water in silicate glass: ^{17}O NMR of hydrous silica, albite, and $Na_2Si_4O_9$ glasses. J. Phys. Chem. B 102 (39), 7523–7529.
Magaritz, M., Hofmann, A.W., 1978. Diffusion of Sr, Ba and Na in obsidian. Geochim. Cosmochim. Acta 42 (6), 595–605.
Maneta, V., Baker, D.R., 2014. Exploring the effect of lithium on pegmatitic textures: an experimental study. Am. Mineral. 99 (7), 1383–1403.
Mills, K.C., Hayashi, M., Wang, L., Watanabe, T., 2014. The structure and properties of silicate slags. Treatise on Process Metallurgy 1, 149–286.
Mungall, J.E., 2002. Empirical models relating viscosity and tracer diffusion in magmatic silicate melts. Geochim. Cosmochim. Acta 66 (1), 125–143.
Mysen, B.O., 2007. The solution behavior of H_2O in peralkaline aluminosilicate melts at high pressure with implications for properties of hydrous melts. Geochim. Cosmochim. Acta 71 (7), 1820–1834.
Mysen, B.O., Virgo, D., Seifert, F.A., 1982. The structure of silicate melts: implications for chemical and physical properties of natural magma. Rev. Geophys. 20 (3), 353–383.
Neukampf, J., Laurent, O., Tollan, P., Bouvier, A.-S., Magna, T., Ulmer, P., France, L., Ellis, B.S., Bachmann, O., 2022. Degassing from magma reservoir to eruption in silicic systems: the Li elemental and isotopic record from rhyolitic melt inclusions and host quartz in a Yellowstone rhyolite. Geochim. Cosmochim. Acta 326, 56–76.
Newman, S., Lowenstern, J.B., 2002. VolatileCalc: a silicate melt–H_2O–CO_2 solution model written in Visual Basic for excel. Comput. Geosci. 28 (5), 597–604.
Ni, H., 2012. Compositional dependence of alkali diffusivity in silicate melts: Mixed alkali effect and pseudo-alkali effect. Am. Mineral. 97 (1), 70–79.
Ni, H., Hui, H., Steinle-Neumann, G., 2015. Transport properties of silicate melts. Rev. Geophys. 53 (3), 715–744.
Ni, P., Zhang, Y., Fiege, A., Newville, M., Lanzirotti, A., 2021. Rapid reduction of basaltic glasses in piston-cylinder experiments: a XANES study. Contrib. Miner. Petrol. 176 (2), 1–18.
O'Connor, P., Gallagher, V., Kennan, P., 1991. Genesis of lithium pegmatites from the Leinster Granite margin, southeast Ireland: geochemical constraints. Geol. J. 26 (4), 295–305.
Papale, P., Moretti, R., Barbato, D., 2006. The compositional dependence of the saturation surface of H_2O + CO_2 fluids in silicate melts. Chem. Geol. 229 (1–3), 78–95.
Provenzano, V., Boesch, L., Volterra, V., Moynihan, C., Macedo, P., 1972. Electrical relaxation in $Na_2O\cdot 3SiO_2$ glass. J. Am. Ceram. Soc. 55 (10), 492–496.
Roselieb, K., Jambon, A., 1997. Tracer diffusion of potassium, rubidium, and cesium in a supercooled jadeite melt. Geochim. Cosmochim. Acta 61 (15), 3101–3110.
Shamloo, H.I., Till, C.B., 2019. Decadal transition from quiescence to supereruption: petrologic investigation of the Lava Creek Tuff, Yellowstone Caldera. WY. Contrib. Mineral. Petrol. 174 (4), 1–18.
Shannon, R.D., 1976. Revised effective ionic radii and systematic studies of interatomic distances in halides and chalcogenides. Acta Crystallogr. Sect. A: Cryst. Phys., Diffr., Theor. Gen. Crystallogr. 32 (5), 751–767.
Sowerby, J.R., Keppler, H., 2002. The effect of fluorine, boron and excess sodium on the critical curve in the albite–H_2O system. Contrib. Miner. Petrol. 143 (1), 32–37.
Spallanzani, R., Koga, K.T., Cichy, S.B., Wiedenbeck, M., Schmidt, B.C., Oelze, M., Wilke, M., 2022. Lithium and boron diffusivity and isotopic fractionation in hydrated rhyolitic melts. Contrib. Miner. Petrol. 177 (8), 1–17.
Tavazzani, L., Peres, S., Sinigoi, S., Demarchi, G., Economos, R., Quick, J., 2020. Timescales and mechanisms of crystal-mush rejuvenation and melt extraction recorded in permian plutonic and volcanic rocks of the sesia magmatic system (Southern Alps, Italy). J. Petrol. 61 (5), egaa049.
Teng, F.-Z., McDonough, W.F., Rudnick, R.L., Walker, R.J., 2006. Diffusion-driven extreme lithium isotopic fractionation in country rocks of the Tin Mountain pegmatite. Earth Planet. Sci. Lett. 243 (3–4), 701–710.
Till, C.B., Vazquez, J.A., Boyce, J.W., 2015. Months between rejuvenation and volcanic eruption at Yellowstone caldera, Wyoming. Geology 43 (8), 695–698.
Troch, J., Huber, C., Bachmann, O., 2022. The physical and chemical evolution of magmatic fluids in near-solidus silicic magma reservoirs: Implications for the formation of pegmatites. Am. Mineral. 107 (2), 190–205.
Van der Laan, S., Zhang, Y., Kennedy, A.K., Wyllie, P.J., 1994. Comparison of element and isotope diffusion of K and Ca in multicomponent silicate melts. Earth Planet. Sci. Lett. 123 (1–3), 155–166.
Vlastélic, I., Menard, G., Gannoun, A., Piro, J.-L., Staudacher, T., Famin, V., 2013. Magma degassing during the April 2007 collapse of Piton de la Fournaise: the record of semi-volatile trace elements (Li, B, Cu, In, Sn, Cd, Re, Tl, Bi). J. Volcanol. Geoth. Res. 254, 94–107.
Watson, E.B., 1979. Diffusion of cesium ions in H_2O-saturated granitic melt. Science 205 (4412), 1259–1260.
Watson, E.B., 1981. Diffusion in magmas at depth in the Earth: the effects of pressure and dissolved H_2O. Earth Planet. Sci. Lett. 52 (2), 291–301.
Zajacz, Z., Halter, W.E., Pettke, T., Guillong, M., 2008. Determination of fluid/melt partition coefficients by LA-ICPMS analysis of co-existing fluid and silicate melt inclusions: controls on element partitioning. Geochim. Cosmochim. Acta 72 (8), 2169–2197.
Zhang, Y., 2010. Diffusion in minerals and melts: theoretical background. Rev. Mineral. Geochem. 72 (1), 5–59.
Zhang, Y., Behrens, H., 2000. H_2O diffusion in rhyolitic melts and glasses. Chem. Geol. 169 (1–2), 243–262.
Zhang, Y., Ni, H., Chen, Y., 2010. Diffusion data in silicate melts. In: Zhang, Y., Cherniak, D. (Eds.), Rev. Mineral. Geochem. pp. 311-408.
Zhang, Y., Ni, H., 2010. Diffusion of H, C, and O components in silicate melts. Rev. Mineral. Geochem. 72 (1), 171–225.
Zotov, N., Keppler, H., 1998. The influence of water on the structure of hydrous sodium tetrasilicate glasses. Am. Mineral. 83 (7–8), 823–834.